Journal of Computational Chemistry

RESEARCH ARTICLE

Influence of Ligand Complexity on the Spectroscopic Properties of Type 1 Copper Sites: A Theoretical Study

Umut Ozuguzel[1] | Serzat Safaltin[2] | S. Pamir Alpay[2,3] | Kenda Alkadry[1] | Reed Nieman[4] | Carol Korzeniewski[4] | Adelia J. A. Aquino[5]

[1]Department of Chemistry, University of Connecticut, Stamford, Connecticut, USA | [2]Department of Materials Science and Engineering and Institute of Materials Science, University of Connecticut, Storrs, Connecticut, USA | [3]Department of Physics, University of Connecticut, Storrs, Connecticut, USA | [4]Department of Chemistry and Biochemistry, Texas Tech University, Lubbock, Texas, USA | [5]Department of Mechanical Engineering, Texas Tech University, Lubbock, Texas, USA

Correspondence: Umut Ozuguzel (umut.ozuguzel@uconn.edu) | Adelia J. A. Aquino (adelia.aquino@ttu.edu)

Received: 22 September 2024 | **Revised:** 5 December 2024 | **Accepted:** 6 December 2024

Funding: This work was supported by the National Science Foundation (CBET-1922956).

Keywords: charge transfer | multi-copper oxidases | resonance Raman | TDDFT | vertical excitation

ABSTRACT

Multi-copper oxidases (MCOs) are enzymes of significant interest in biotechnology due to their efficient catalysis of oxygen reduction to water, making them valuable in sustainable energy production and bio-electrochemical applications. This study employs time-dependent density functional theory (TDDFT) to investigate the electronic structure and spectroscopic properties of the Type 1 (T1) copper site in Azurin, which serves as a model for similar sites in MCOs. Four model complexes of varying complexity were derived from the T1 site, including 3 three-coordinate models and 1 four-coordinate model with axial methionine ligation, to explore the impact of molecular branches and axial coordination. Calculations using ωB97X-D3 functional, def2-TZVP basis set, and conductor-like polarizable continuum model (CPCM) solvation model reproduced key experimental spectral features, with increased model complexity improving agreement, particularly for the ~400 cm^{-1} band splitting in resonance Raman spectra. This work enhances our understanding of T1 copper sites' electronic properties and spectra, bridging the gap between simplified models and complex proteins. The findings contribute to the interpretation of spectroscopic data in blue copper proteins and may inform future studies on similar biological systems.

1 | Introduction

Multi-copper oxidases (MCOs) are a class of enzymes that play crucial roles in biological electron transfer processes and have gained significant attention for their potential applications in biotechnology. These enzymes are characterized by their ability to catalyze the four-electron reduction of molecular oxygen to water, making them highly efficient and environmentally friendly catalysts [1–3]. This unique property has led to their increasing importance in the development of energy and chemical sensing technologies, where MCOs are often used as cathode catalysts [4–7], as well as in biosensors and other bio-electrochemical applications [8]. The functionality of MCOs is centered on multiple copper sites, notably the Type 1 (T1) copper site and the trinuclear copper cluster (TNC). The T1 site acts as the primary electron acceptor from the substrate and is responsible for shuttling these electrons to the TNC. At the TNC, the transferred electrons reduce molecular oxygen to water, completing the catalytic cycle [1, 3, 9–11].

Raman spectroscopy has emerged as a powerful tool for probing the electronic structure of T1 centers, providing valuable insights into their vibrational modes and metal–ligand interactions [1, 12–19]. Recent advancements in experimental techniques have enabled the study of an MCO within a bioelectrocatalytic membrane using Raman spectroscopy [20]. While the experiment provides crucial insights into the behavior of these enzymes, interpreting the complex spectral data remains challenging. To avoid the complexity of the protein spectra, smaller synthetic molecules mimicking the T1 site have been studied experimentally [12, 16, 17, 21–24]. Early computational efforts using primitive models provided initial insights into the electronic structure of these systems [13, 14]. Subsequently, more advanced computational studies have been conducted on both T1 mimics [25] and actual T1 centers from proteins [26, 27], allowing for a more comprehensive understanding of their spectroscopic and electronic properties.

While MCOs are complex multi-copper enzymes, the T1 copper site is also found in simpler, single-domain proteins known as blue copper proteins [28]. Like MCOs, these proteins are characterized by their intense absorption band around 600 nm, which gives them their distinctive blue color [1]. In its oxidized state, the T1 center consists of a Cu^{2+} ion strongly coordinated to one cysteine and two histidine residues in an approximate trigonal planar arrangement, sometimes with additional weak axial ligand interactions [29–33]. Among the blue copper proteins, the wild-type (WT) Azurin T1 site has emerged as a valuable model system for structural and spectroscopic studies [18, 26, 34, 35]. Figure 1A shows a structural model of *Pseudomonas aeruginosa* azurin that highlights the interactions of the strong coordinating ligands around the Cu^{2+} site (three weakly coordinating axial residues; a methionine (MET) a phenylalanine (PHE), and a glycine (GLY) have been omitted for clarity) [36]. The model depicted has been widely used to study the T1 copper site, as its protein backbone, and copper site geometry closely resemble those of the wild type Azurin [27, 38, 39]. The relative simplicity of Azurin, its well-characterized T1 site structure, robust stability, and lack of additional metal centers makes it an ideal candidate for both experimental and computational investigations [27, 40–45].

In this study, the T1 copper site of Azurin is systematically modeled through four complexes of varying complexity to investigate the impact of molecular branches on spectroscopic properties. The models include both 3- and 4-coordinated copper geometries, with the latter incorporating the axial methionine ligand to better represent the complete coordination environment observed in X-ray structures. The histidine residues HIS 46 and HIS 117 are truncated to imidazole (Im) groups, designated as Im$_1$ and Im$_2$, respectively, while the cysteine residue is truncated at different points along its peptide bonds to systematically examine the influence of molecular branching on electronic and spectroscopic properties. The weak backbone interactions from PHE 114 and GLY 46 (Figure 1B) were excluded from this study, as their contributions to the electronic properties and spectroscopic features of the T1 copper site are expected to be minimal compared to the direct coordinating ligands. This approach allows us to systematically evaluate how the equatorial primary coordination sphere ligands and methionine axial ligation influence the characteristic spectroscopic features of T1 copper sites, while maintaining computational tractability. The models incorporate increasing molecular complexity to better represent the steric and electronic environment of the protein-bound copper center, providing insights into how structural features influence spectroscopic properties. Figure 2 depicts the distinct truncated models Im$_2$CuSL, each characterized by the thiolate ligand, where L is either a methyl group (Me), a RH$_2$(R′) group, where R is CH$_2$-C and R′ is NHCO-CH$_3$ or an RH(R′)(R″) group, where R″ is CONH-CH$_3$.

These R′ and R″ groups represent truncations at the C- and N-termini (Figure 2) of the peptide bonds from the cysteine residue, respectively. A thorough analysis of these truncates is conducted using geometry optimizations, time-dependent density functional theory (TDDFT) calculations, and charge transfer analysis. The simulated electronic absorption and resonance Raman (RR) spectra agree well with experimental data [27, 40], providing insights into the optically driven electronic and vibrational

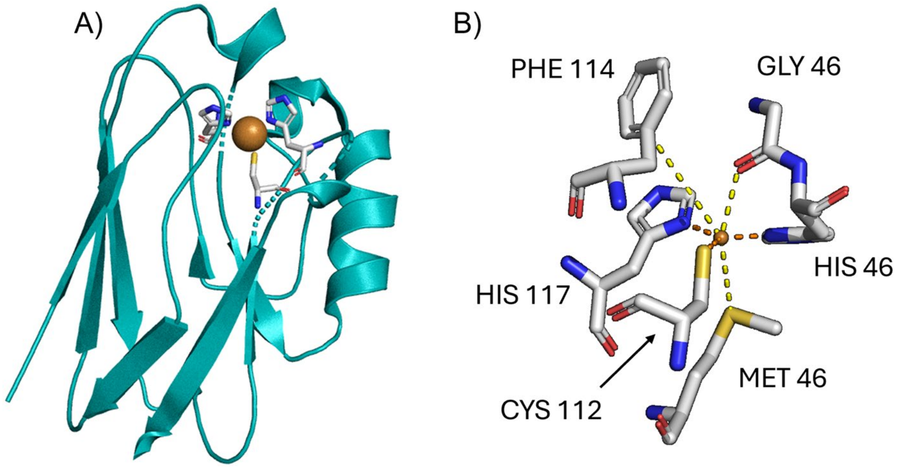

FIGURE 1 | (A) The structure of WT Azurin [36] highlighting the T1 copper site. The direction of the arrows shows the sequence from N-terminus to C-terminus. (B) A zoomed-in view of the T1 copper site in WT Azurin. The following structures are indicated: protein residues (teal), carbon atoms (gray), oxygen atoms (red), nitrogen atoms (blue), copper atom (orange), and sulfur atom (yellow). Histidine (HIS) 46, HIS 117, cysteine (CYS) 112, glycine (GLY) 46, phenylalanine (PHE) 114, and methionine (MET) 46 are labeled to indicate the residues coordinated with the copper ion. The dashed orange lines represent stronger interactions between Cu–S(Cys) and Cu–N(His) residues, and the yellow lines represent weaker axial interactions between Cu–S(MET), Cu–C(PHE), and Cu–O(GLY). Adapted from the Protein Data Bank structure PDB:1JZF [37].

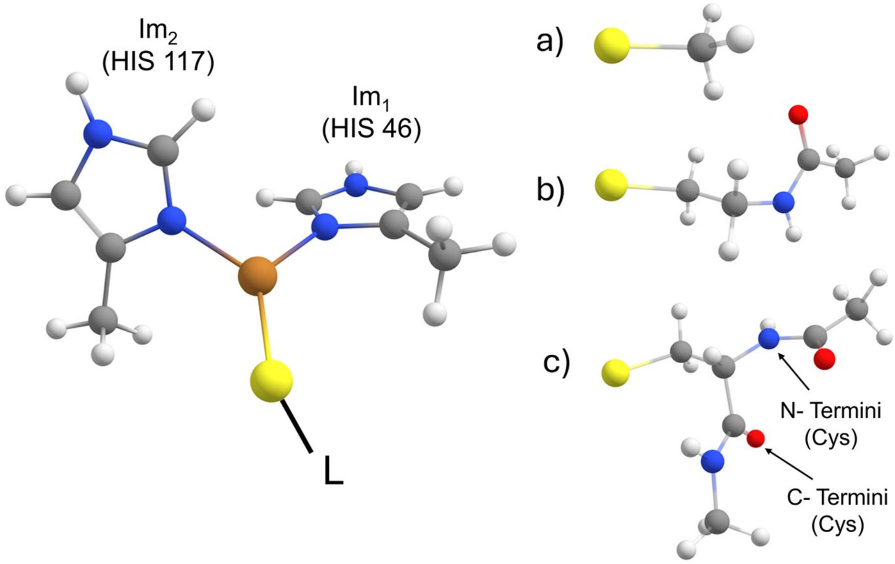

FIGURE 2 | Truncated models for the T1 copper site of wild-type Azurin distinguished by the thiolate ligand S- L for (a) S-Me, where Me represents a methyl group, (b) S-RH2(R'), where R is CH_2-C and R' is NHCO-CH_3 (N-Termini) and (c) S-RH(R')(R″), where R″ is CONH-CH_3 (C-Termini). Imidazole (Im) groups used as a model for HIS 117 and HIS 466. Colors: Hydrogen—White, Carbon—Gray, Nitrogen—Blue, Oxygen—Red, Copper—Orange, Sulfur—Yellow.

transitions. This work aims to bridge the gap between simplified models and complex proteins, enhancing our understanding of electron transfer in blue copper proteins. The insights derived from this study are expected to inform future research on multicopper oxidases and contribute to the advancement of bio-inspired technologies for sustainable energy applications.

2 | Computational Details

Ground state geometry optimizations were performed using the long-range corrected ωB97X-D3 hybrid exchange functional [46] in combination with the def2-TZVP triple-zeta valence polarization basis set [47]. The resolution of identity (RI) approximation [48] was implemented for two-electron integrals to enhance computational efficiency. Environmental effects were accounted for using the conductor-like polarizable continuum model (CPCM) [49], simulating aqueous conditions with a dielectric constant of $\varepsilon = 80.4$ and a refractive index of $n = 1.33$. Vibrational frequencies were computed within the harmonic oscillator approximation to confirm that optimized structures corresponded to true energy minima. The Im_2CuS[RH(R')(R″)]—MET model shows a single negative frequency at $-27\,cm^{-1}$ due to the constrained distance between the S(MET)–Cu bond. Cartesian coordinates of these optimized geometries are provided in the Supporting Information (SI).

For excited state properties, TDDFT [50] method was employed. Vertical excitation energies for the first ten doublet states were computed assuming non-equilibrium solvent conditions. Electronic absorption spectra were generated using a Gaussian band shape with a $1000\,cm^{-1}$ full width at half maximum (FWHM). Normal Raman spectra were derived from ground state electronic properties, while RR spectra were computed using the vertical gradient (VG) method [51–55] for bright states and plotted with a Voigt band shape ($10\,cm^{-1}$ effective FWHM).

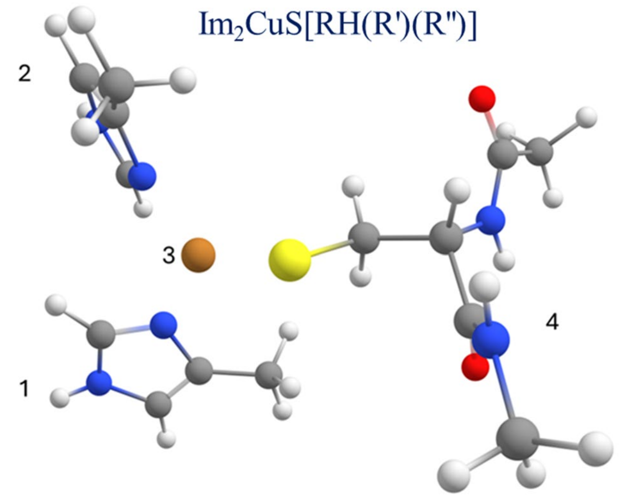

FIGURE 3 | Schematic representation of the S-RH(R')(R″) model illustrating the four fragments used in the charge transfer analysis: Imidazole 1 (Fragment 1), imidazole 2 (Fragment 2), Cu atom (Fragment 3), and thiolate ligand (Fragment 4). This fragmentation scheme is representative of the approach for calculating qCT values.

In all cases, qCT [56] values were calculated with reference to four distinct fragments: the imidazole (Im) groups Im_1 and Im_2 (Fragments 1 and 2), the Cu atom (Fragment 3), and the thiolate ligand (Fragment 4). Figure 3 illustrates these fragments using the S-RH(R')(R″) model as an example, which is representative of the fragmentation scheme applied to all models in this study. Figure S1 in the SI shows the fragments for all models.

The ORCA program suite (version 5.0.4) [57] was used for all quantum chemical calculations in this study. The TheoDORE program suite [56, 58, 59] was used for analysis of charge transfer (qCT) characteristics through examination of transition density matrices [56] and natural transition orbitals (NTOs) [60].

3 | Results and Discussion

3.1 | Ground-State Molecular Structures

The geometries of the three complexes, Im_2CuSMe, $Im_2CuS[RH_2(R')]$, and $Im_2CuS[RH(R')(R'')]$ (hereafter also referred to as S-Me, $S\text{-}RH_2(R')$, and S-RH(R')(R″), respectively), were optimized under implicit solvation conditions without constraints, to investigate the subtle variations in vibrational and electronic structures induced by different thiolate ligands around the T1 Cu site. Additionally, the geometry of $Im_2CuS[RH(R')(R'')]$—MET (S-RH(R')(R″)—MET) was optimized under implicit solvation conditions, and a distance restraint was applied to Cu and S(MET) to maintain the 3.317 Å distance between the metal ion and the methionine residue.

Table 1 presents the optimized Cu(II)-ligand bond lengths, compared with data from the X-ray crystal structure of *P. aeruginosa* azurin [36] in its oxidized state. In the methyl–thiolate complex, the imidazole groups exhibit slightly different copper–nitrogen bond lengths, with Cu–Im_1 being marginally longer than Cu–Im_2. This pattern continues in the singly substituted R-thiolate complex, where both Cu–N bonds decrease slightly but maintain their relative lengths. Interestingly, in the doubly substituted R-thiolate complex, this trend reverses, with the Cu–N bond for Im_2 becoming slightly longer than Im_1, mirroring the pattern observed in the crystal structure. The calculated Cu–S and Cu–N bond distances in the three-coordinate models are consistently shorter than the experimental values obtained from crystal structure data [36]. The incorporation of the axial methionine ligand in S-RH(R')(R″)-MET results in a modest elongation of the equatorial Cu–N bonds, enhancing the agreement with the experimental geometry [33]. However, some discrepancies remain due to the lack of weak axial interactions from the primary sphere (PHE and GLY, Figure 1B), as well as secondary sphere interactions such as hydrogen-bonding networks and protein backbone constraints. Additionally, the long-range effects from the protein present in the native structure also contribute to these differences. Among the models, both the S-RH(R')(R″) and S-RH(R')(R″)-MET structures show good agreement with the experimental bond distances, with the four-coordinate model providing the closest match to the crystal structure geometry. This improved accuracy stems from both the increased structural complexity of the thiolate ligand and the inclusion of axial coordination, which better mimics the complete coordination environment of the protein-bound T1 Cu site.

TABLE 1 | Calculated Cu–S and Cu–N bond distances for the three truncated T1 copper site models considered ($Im_2CuS[Me]$, $Im_2CuS[RH_2(R')]$, and $Im_2CuS[RH(R')(R'')]$) in comparison to those of wild-type Azurin.[a,b]

Structures	Cu–S	Cu–N$(Im)_1$	Cu–N$(Im)_2$
$Im_2CuS[Me]$	2.130	1.972	1.970
$Im_2CuS[RH_2(R')]$	2.126	1.970	1.968
$Im_2CuS[RH(R')(R'')]$	2.145	1.964	1.966
$Im_2CuS[RH(R')(R'')]$—MET	2.138	1.971	1.970
Azurin Crystal Structure (PDB: 1JZF)[b]	2.205	2.020	2.080

[a] Distances are reported in Å.
[b] Azurin structure taken from Ref. [36].

Table S1 presents the bond angles surrounding the Cu^{+2} ion for all T1 copper site models. Since all models were optimized without the constraints imposed by the protein structure, some deviations from experimental values are expected. The N–Cu–N angle remains consistent across all computational models, slightly underestimating the experimental value. Importantly, the S-RH(R')(R″) model most accurately reproduces the $N(Im)_1$–Cu–S angle observed in the crystal structure, while the S-Me and $S\text{-}RH_2(R')$ models show slight deviations. The S-RH(R')(R″)—MET model shows a slightly larger angle. For the $N(Im)_2$–Cu–S angle, both R-thiolate models ($S\text{-}RH_2(R')$ and S-RH(R')(R″)) follow the experimental trend of being smaller than the $N(Im)_1$–Cu–S angle, with S- RH(R')(R″)—MET matching the crystal structure value precisely. However, the S-Me model deviates from this pattern, exhibiting a slightly larger $N(Im)_2$–Cu–S angle. The dihedral angle Cu–S–C_1–C_2, relevant only for the R-thiolate models, shows variation among the models, with S-RH(R')(R″)—MET providing the closest match to the experimental value, followed by S-RH(R')(R″) [36].

The enhanced geometric accuracy in the more complex truncated T1 copper site models is due to their bulkier thiolate groups, which better replicates the steric environment of the protein. These bulky substituents curve toward the $N(Im)_1$ group, mimicking the spatial arrangement of the native protein, leading to a closer match with experimental structure. This makes the R-thiolate models more suitable for further spectroscopic studies compared to the simpler methyl-thiolate model. Additionally, the R-substituents in these models influence the Cu–S–C_1–C_2 dihedral angles, aligning them closely with the experimental structure. Overall, the S-RH(R')(R″) and S-RH(R')(R″)—MET models demonstrates the closest alignment with the crystal structure data across multiple geometric parameters, suggesting its enhanced ability to capture the nuances of the T1 copper site.

3.2 | Excited States, Transition Orbitals, and Omega Matrices

Table 2 presents the vertical excitation energies, oscillator strengths, and charge transfer (qCT) quantities for the 10 lowest doublet excited states of the S-RH(R')(R″) model. Corresponding data for the S-Me, S- $RH_2(R')$, and S-RH(R')(R″)—MET models are available in the Supporting Information (Tables S2–S4).

Examination of the oscillator strengths for S-RH(R')(R″) reveals a single prominent bright state, D_5 at 1.944 eV (Table 2). This state is particularly relevant to the RR process, as discussed in subsequent sections. The natural transition orbital (NTO) for D_5, illustrated in Figure 4, demonstrates significant involvement of both S and Cu atoms in the electronic transition. States D_1 and D_5–D_9 exhibit qCT values exceeding 0.5 *e*, indicative of substantial intramolecular charge transfer between the model's fragments.

Figure 5 displays omega matrices, which provide a concise representation of the excitation processes. For S-RH(R')(R″), the

TABLE 2 | Calculated vertical excitation energies, oscillator strengths, and charge transfer values for the first 10 electronic states of S-RH(R′)(R″) model, compared with experimental molar absorptivity.[a,b]

Excited states	ΔE/eV[a] (nm)	f	qCT (e)	ΔE/eV[a,b] (nm)	ε ($M^{-1}cm^{-1}$)
D_1	0.865 (1434)	0.000	0.533	0.673 (1842)	nd
D_2	1.66 (747)	0.001	0.467	1.327 (935)	nd
D_3	1.796 (690)	0.001	0.472	1.562 (794)	730
D_4	1.854 (669)	0.002	0.464	1.699 (730)	740
D_5	1.944 (638)	0.151	0.594	1.971 (629)	5070
D_6	3.001 (413)	0.000	0.534	2.244 (553)	510
D_7	3.543 (350)	0.001	0.933	2.492 (498)	160
D_8	3.669 (338)	0.000	0.936		
D_9	4.511 (275)	0.002	0.582		
D_{10}	4.536 (274)	0.000	0.034		

[a] ΔE in eV and (in parentheses) nm units.

[b] Experimental electronic absorbance spectrum of Azurin, values from the ref [27]; nd, not determined.

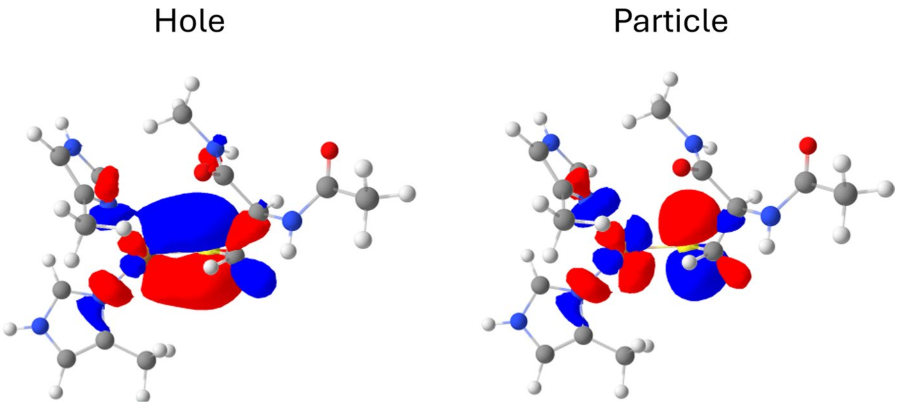

FIGURE 4 | Natural transition orbital (NTO) for excited state D_5 of the S-RH(R′)(R″) model in its ground state geometry. The iso-surface value is set at ±0.03 e/Bohr^3.

first four excited states (D_1–D_4), show electron localization primarily on the Cu atom with some charge transfer to the thiolate ligand. The bright state D_5, and the states D_6 and D_9 exhibit charge transfer from the thiolate ligand to Cu^{2+}, with some local excitations on the thiolate ligand. D_7 and D_8 demonstrate charge transfer from imidazole groups to both Cu and the thiolate ligand, while D_{10} shows minimal charge transfer activity.

The S-Me and S-RH_2(R′) models display similar characteristics, with D_5 as the bright state in both cases. For these models, the absorption energies are 1.927 and 1.934 eV (Table 2), respectively, while the qCT values are approximately 0.6 e. The omega matrices for these models (Figures S2 and S3) reveal patterns that are comparable to S-RH(R′)(R″), with slight variations in S-Me. The four-coordinate S-RH(R′)(R″)-MET model introduces an additional fragment (Fragment 5, methionine, Figure S4) while maintaining similar electronic characteristics. The lower energy states (D_1–D_4) display strong localized Cu excitations, with excitation energies ranging from 0.863 to 1.811 eV and moderate qCT values (~0.47–0.54 e). The bright state D_5, at 2.017 eV, exhibits a mixed character with local Cu excitation and charge transfer from the thiolate ligand (Fragment 4) to Cu, with qCT value of 0.577 e. In the higher energy region, D_6 (3.008 eV) shows similar qCT characteristics (0.537 e) to D_5, while D_7–D_9 demonstrate strong charge transfer character (qCT > 0.93 e). D_7 shows charge transfer from methionine (Fragment 5) to Cu, D_8 and D_9 involve charge transfer from the imidazole groups (Fragments 1 and 2) to Cu. The highest energy state D_{10} (4.526 eV) exhibits moderate charge transfer (qCT = 0.588 e) from the thiolate ligand (Fragment 4) to Cu. These results demonstrate how axial methionine coordination influences the electronic structure by providing additional ligand-to-metal charge transfer pathways.

NTOs for the bright states of all models (Figures 4, S5–S7) consistently show "bonding" hole density and "anti-bonding" electron density with respect to the Cu–S bond, reflecting contributions from the HOMO and LUMO. The S-RH(R′)(R″)-MET model (Figure S7) maintains this characteristic Cu–S bonding pattern, with no significant contribution from the axial methionine ligand to the bright state transition. These findings align with experimental assignments of bright state transitions and

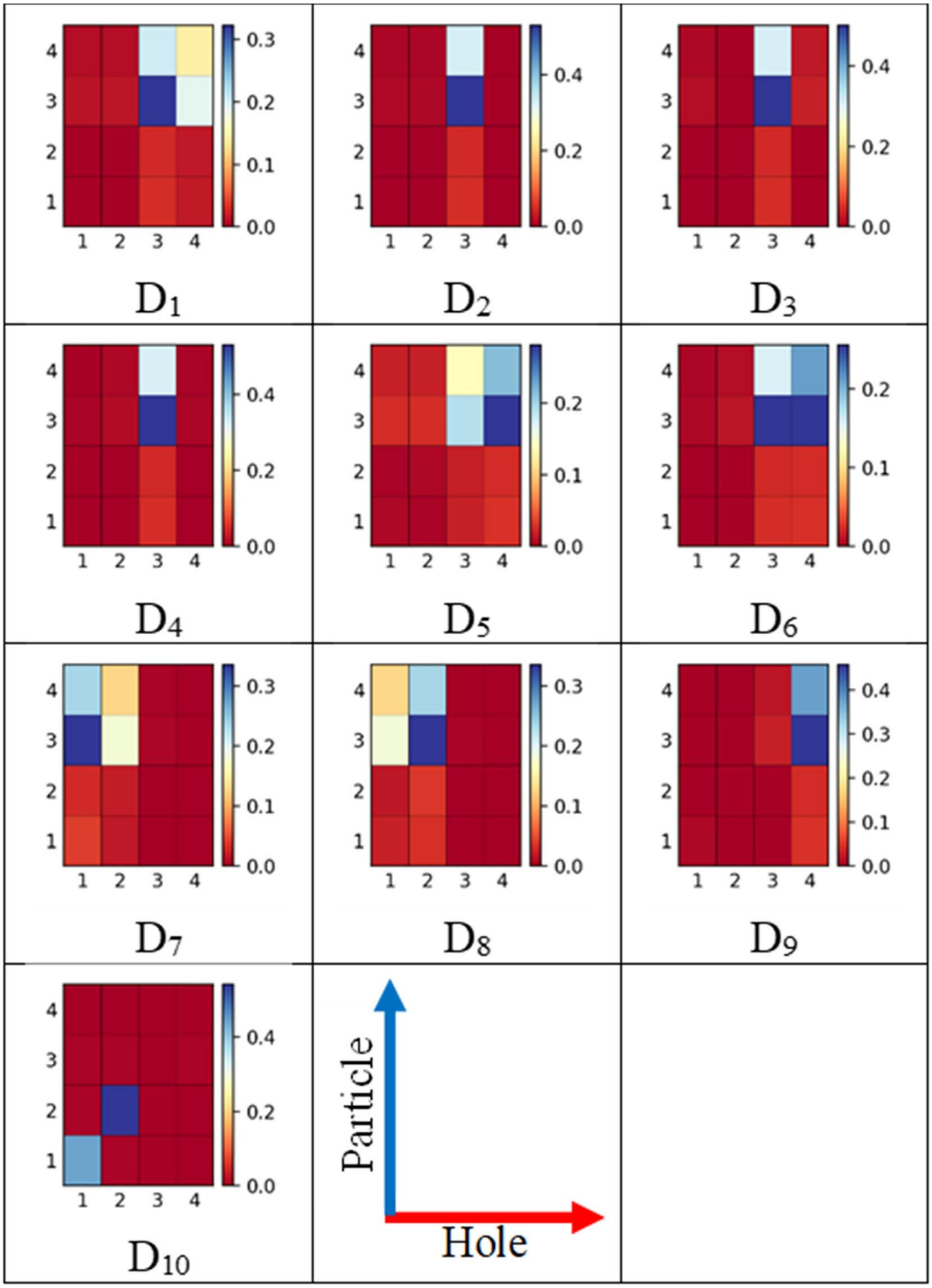

FIGURE 5 | Omega matrices for excited states D_1–D_{10} of the S-RH(R')(R″) model in its ground state geometry. The horizontal and vertical axes correspond to hole and electron states for fragments 1 to 4, with blue regions denoting the highest charge transfer activity.

previous studies on T1 site mimics [13, 14, 23, 25]. For completeness, NTOs for the remaining nine excited states of S-RH(R')(R″) are provided in Figure S8.

3.3 | Electronic Absorption Spectra

The electronic absorption properties of blue copper proteins are fundamental to their spectroscopic characterization, particularly in RR investigations. To elucidate these properties, simulations of the electronic absorption spectra for all the T1 copper site models were performed. Figure 6 presents a comparative analysis between the computed spectrum of the S-RH(R')(R″) T1 model and the experimentally obtained spectrum of wild-type Azurin [27].

The analysis of the calculations encompasses transitions from the ground state to the first 10 electronic excited states (see Table 2). To facilitate direct comparison, both spectra have

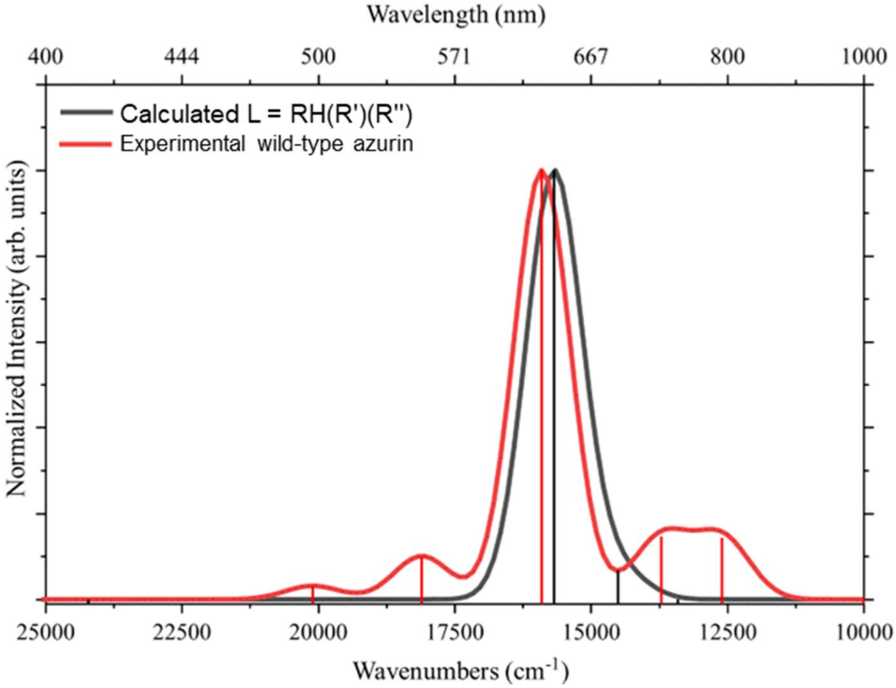

FIGURE 6 | Comparison of the S-RH(R′)(R″) model calculated electronic absorption spectrum (black line) with the experimental electronic absorption spectrum of wild-type Azurin (red line) [27]. The calculated oscillator strengths and experimental molar absorptivity values have been normalized for direct comparison and are presented in arbitrary units (arb. units).

been normalized to their respective maximum intensity wavelengths. The experimental Azurin spectrum [27] exhibits a bright state assigned to an S p$\pi \rightarrow Cu^{2+}$ transition, corresponding to excited state D_5 at 629 nm. The predicted bright state for S-RH(R′)(R″) is also D_5, at 638 nm, representing a transition from a bonding to an anti-bonding state localized on the Cu–S bond, accompanied by charge transfer from the thiolate ligand to Cu^{2+} (see Figure 5 and Table 2), as discussed in Section 3.2. A notable discrepancy arises in the secondary transition. The experimental absorption spectrum [27] reveals two lower intensity transitions attributed to D_3 and D_4 at 790 and 730 nm, respectively. The four-coordinate model including the axial methionine ligand (Table S4, Figure S9) exhibits corresponding features: a weak transition at 798 nm and a more intense transition at 688 nm, showing improved agreement with the experimental spectrum compared to the three-coordinate models. The remaining differences in peak positions and intensities can be attributed to several factors in the protein environment. As illustrated in Figure 1B, the T1 copper site in the protein contains both equatorial and axial ligands in the primary coordination sphere [33]. The weak axial interactions from PHE 114, which can provide donor–acceptor interactions with HIS 117 and the axial oxygen of GLY 46 which forms ionic interactions between its carbonyl oxygen and the copper [33] were not included in the model. The conformational constraints imposed on the CYS residue also may contribute. In the computational models, the structure was allowed to relax during geometry optimization, whereas in the actual protein, the conformation is restricted by the surrounding amino acids and protein structure, as illustrated by the comparison of the protein and model structures in Figure S10. Additionally, secondary sphere interactions such as hydrogen bonding networks, as well as the long-range effects from the protein, affect the electronic structure and, consequently, the observed spectral features.

The smaller complexity models, S-Me and S-RH_2(R′), exhibit analogous spectral features, as illustrated in Figures S11 and S12 of the SI, respectively. These models demonstrate bright states at 617 and 605 nm, respectively (Tables S2 and S3). Notably, the S-Me model, despite being the least complex, shows an absorption maximum between those of S-RH_2(R′) and S-RH(R′)(R″). This non-linear relationship between model complexity and absorption maximum underscores the subtle interplay of electronic effects in these T1 copper site models.

3.4 | RR Spectra

In alignment with experimental limitations and the most relevant spectral features, the computational analysis of RR spectra focuses primarily on the vibrational modes below 900 cm^{-1} [27, 40, 41]. This spectral range encompasses the key structural information pertinent to the T1 copper site. Figure 7 presents a comparative analysis of the calculated normal and RR spectra for the S-Me model, excited at 1300 and 647 nm, respectively. The spectra are plotted on an absolute Raman activity scale. To facilitate comparison, the off-resonance spectrum has been amplified by a factor of ~10^4. This amplification enhances peak intensities at 397 and 794 cm^{-1} in the resonance spectrum, with intensities approximately 10^4 times greater than their off-resonance counterparts.

Analysis of the normal mode displacements indicates that the 397 cm^{-1} vibration is predominantly characterized by Cu–S stretching. This observation aligns with theoretical predictions of strong RR scattering from vibrational modes with

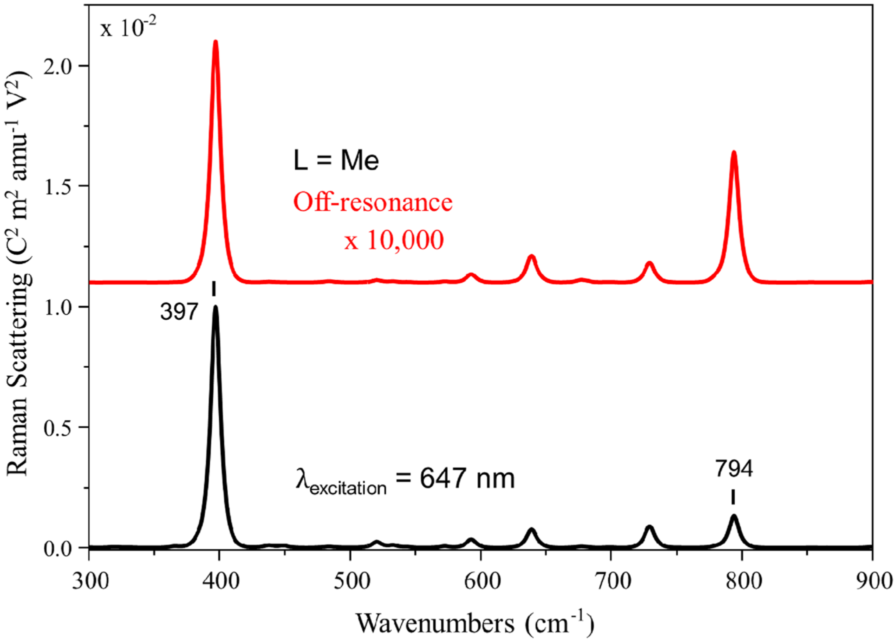

FIGURE 7 | Simulated off-resonance (top, red) and resonance Raman (bottom, black) spectra for the S-Me model, calculated at excitation wavelengths of 1300 and 647 nm, respectively. The Raman intensities are plotted in units of $C^2\ m^2\ amu^{-1}\ V^2$. The scale of the off-resonance Raman spectrum has been amplified by a factor of ~10^4.

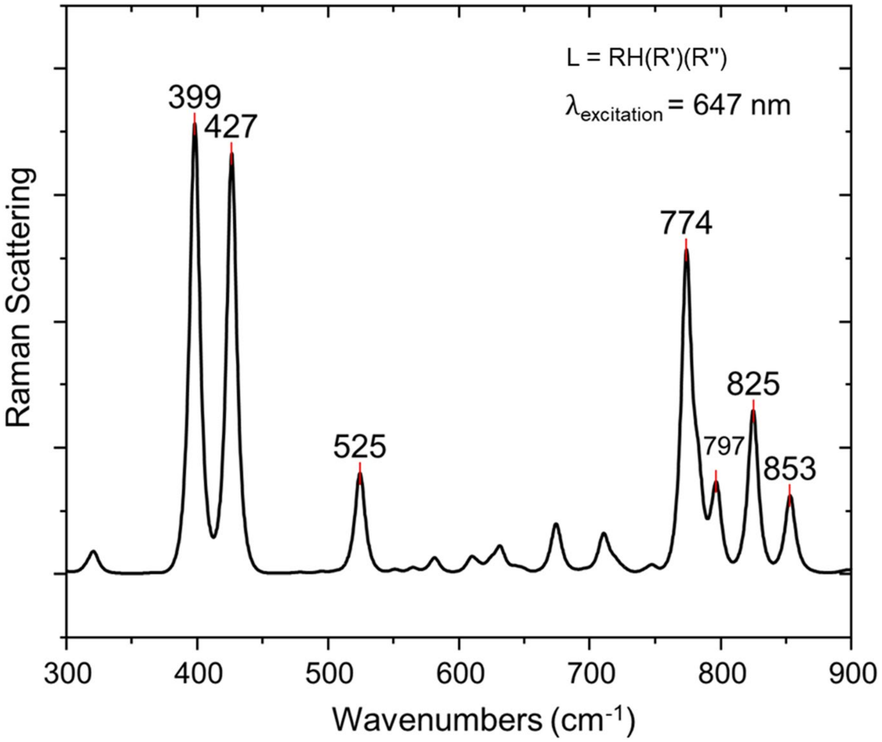

FIGURE 8 | Simulated resonance Raman spectrum for the S-RH(R′)(R″) model, plotted over the region of interest.

significant Cu–S stretching components upon excitation of the S pπ → Cu^{2+} charge transfer transition. The normalized RR spectrum of the S-RH_2(R′) model, depicted in Figure S13, exhibits similar characteristics to the S-Me model, with a single prominent band in the ~400 cm^{-1} region, albeit shifted to 412 cm^{-1}. In the higher energy region, the band at 783 cm^{-1} is attributed to S–C stretching coupled with C–C–N bending modes, likely originating from the coordinated cysteine residue. Unlike the S-Me model, the S-RH_2(R′) spectrum has a single overtone band at 828 cm^{-1}.

The RR spectrum of the more complex S-RH(R′)(R″) model is shown in Figure 8. Most notably, the strong band in the ~400 cm^{-1} region splits into two bands in both the S-RH(R′)(R″)

TABLE 3 | Calculated normal vibrational modes and their assignments for the S-RH(R′)(R″) model compared with experimental data from wild-type Azurin.[a]

Mode	S-Me	S-RH$_2$(R′)	S-RH(R′)(R″)	S-RH(R′)(R″)—MET	Exp[a]
Cu–S Str.	397 *s*	414 *s*	397 *s*	400 s	372 *s*
			399 *s*	440 m	407 *s*
			427 *s*		425 *s*
Ligand deformation			525 *w*		460 *w*
S-C str.	794 *m*	783 *m*	774 *m*	782 w	748 *w*
Overtones		828 *w*	797 *w*	801 w	780 *w*
			825 *w*	840 w	814 *w*
			853 *w*		

[a] Experimental (Exp) values and mode assignments are from ref [40]. Str, stretching mode and in italics, *s*, strong, *m*, medium, *w*, weak intensities, respectively.

and S-RH(R′)(R″)—MET (Figure S14) models. In the three-coordinate model, these bands appear at 399 and 427 cm^{-1}, while the four-coordinate model shows bands at 400 and 440 cm^{-1} (Figure S10). This splitting phenomenon can be attributed to introducing new vibrational modes resulting from the increased complexity of the thiolate ligand and axial coordination, a feature consistent with those of previously reported T1 mimics [23, 25].

Table 3 provides a comprehensive comparison of significant normal modes for all models alongside experimental modes and their assignments [40]. Detailed examination of the normal modes reveals that both complex models show characteristic Cu–S stretching bands in the ~400 cm^{-1} region. In the S-RH(R′)(R″) model, the lower frequency band originates from two closely spaced modes at 397 and 399 cm^{-1}, both involving Cu–S and Cu–N stretching coupled with imidazole bending vibrations, while the band at 427 cm^{-1} is primarily associated with Cu–S stretching coupled to thiolate ligand deformations. Similarly, the S-RH(R′)(R″)—MET model exhibits a strong Cu–S stretching band at 400 cm^{-1} and a medium intensity band at 440 cm^{-1}. These calculated bands show excellent agreement with their experimental counterparts for wild-type Azurin observed at 372, 407, and 425 cm^{-1} (Table 3), which have been assigned to Cu–S(CYS) and Cu–N(HIS) stretching modes.

The weak band at 525 cm^{-1} is assigned to thiolate ligand bending motions with some Cu–S character. While this band appears to be overestimated compared to the weak experimental band at 460 cm^{-1} (assigned to ligand deformation modes with Cu–S stretching contributions), it may explain the reduced band enhancements observed experimentally in the higher 400 cm^{-1} region [40]. In the higher energy region (~800 cm^{-1}), both S-RH(R′)(R″) and S-RH(R′)(R″)—MET models show enhanced bands. The S-RH(R′)(R″) model exhibits a medium intensity mode at 774 cm^{-1} with strong S-C stretching character, corresponding well with the experimental band at 748 cm^{-1}, and three overtone bands at 797, 825, and 853 cm^{-1}. Similarly, in the S-RH(R′)(R″)—MET model, a weak band at 782 cm^{-1} is identified as S-C stretching vibration, while bands at 801 and 840 cm^{-1} are identified as overtones. These features are consistent with experimental assignments of overtone bands in this region at 780 and 814 cm^{-1}.

Despite minor discrepancies in calculated versus observed band frequencies and intensities, both the S-RH(R′)(R″) and S-RH(R′)(R″)—MET models successfully capture the main spectral features of the T1 copper site. The inclusion of the axial methionine ligand maintains the characteristic vibrational patterns while providing additional insight into the role of axial coordination. This agreement underscores the efficacy of these models in representing the electronic and vibrational properties of the protein active site, providing valuable insights into the structure–spectroscopy relationships in blue copper proteins.

4 | Conclusions

This study presents a comprehensive computational investigation of T1 copper site models with increasing complexity: 3 three-coordinate models (S-Me, S-RH2(R′), and S-RH(R′)(R″)) and 1 four-coordinate model including axial methionine coordination (S-RH(R′)(R″)—MET). The work encompasses ground state geometries, electronic excitations, absorption spectra, and RR spectra, providing valuable insights into the structure–property relationships of blue copper protein active sites.

The ground state geometries of the models are in good agreement with the experimental data, with the closest match achieved by the S-RH(R′)(R″)—MET model (Tables 1 and S1). The inclusion of the axial methionine ligand improves agreement with experimental geometry through modification of the primary coordination sphere bond lengths. This suggests that increasing both the thiolate ligand complexity and coordination number better approximates the T1 copper site structure. Nevertheless, some geometric discrepancies remain due to the absence of weak axial interactions from PHE 114 and GLY 46 residues, along with secondary sphere interactions such as hydrogen-bonding networks and protein backbone constraints.

The electronic absorption calculations successfully reproduce the primary features of experimental spectra, including the prominent S $p\pi \rightarrow Cu^{2+}$ transition (Figure 5). Including the axial methionine ligand in S-RH(R′)(R″)—MET improves agreement with experiment, including the reproduction of a transition at 688 nm that corresponds to the experimental feature at 730 nm. Fully capturing the electronic structure of these complex systems remains challenging as achieving accurate transition energies depends on all primary and secondary sphere interactions within the protein environment. Nevertheless, the consistency across our series of models provides confidence in the overall trends observed (Table S1, Figures S9, S11, S12).

The RR spectra calculations reveal a striking enhancement of Cu–S stretching modes upon resonant excitation, consistent with experimental observations. Notably, the splitting of the ~400 cm^{-1} band appears in both the S-RH(R')(R″) (Figure 8) and S-RH(R')(R″)—MET (Figure S14) models, but is not observed in simpler models, aligns with expectations based on previous experimental and computational studies of T1 mimic sites reported in the literature. This splitting demonstrates the importance of ligand complexity in accurately representing the vibrational properties of the T1 copper site. The agreement between calculated and experimental RR spectra, particularly for the S-RH(R')(R″) and S-RH(R')(R″)—MET models (Table 3), validates our computational approach and provides a solid foundation for future spectroscopic studies of blue copper proteins.

It is important to note that the accuracy of these calculations depends highly on the steric environment around the thiolate ligand. While both three- and four-coordinate models provide valuable insights, the accuracy of these calculations depends on capturing the complete protein environment around the T1 copper site. The presence of the axial methionine ligand improves geometric and spectroscopic agreement with experiment, yet the weak axial interactions from PHE 114 and GLY 46 residues, along with secondary sphere interactions such as hydrogen-bonding networks and protein backbone constraints, remain to be fully addressed. A more comprehensive study could be achieved using QM/MM methods, which would allow for including the entire protein structure without altering the T1 site. This progress will help bridge the gap between theoretical predictions and experimental observations, yielding deeper insights into the structure–function relationships of these fascinating and important proteins. Future work in this direction promises to enhance our understanding of blue copper proteins and their roles in biological electron transfer processes, aiding the development of alternative renewable energy technologies.

Acknowledgments

The computational work performed on this project was done with help from the Storrs High-Performance Computing cluster. We would like to thank the UConn Storrs HPC and HPC team for providing the resources and support that contributed to these results. C.K. acknowledges support from the National Science Foundation (CBET-1922956).

Data Availability Statement

The data that support the findings of this study are available from the corresponding author upon reasonable request.

References

1. S. M. Jones and E. I. Solomon, “Electron Transfer and Reaction Mechanism of Laccases,” *Cellular and Molecular Life Sciences* 72 (2015): 869–883.

2. D. den Boer, H. C. de Heer, F. Buda, and D. G. H. Hetterscheid, “Challenges in Elucidating the Free Energy Scheme of the Laccase Catalyzed Reduction of Oxygen,” *ChemCatChem* 15, no. 1 (2023): e202200878, https://doi.org/10.1002/cctc.202200878.

3. S. Shleev, J. Tkac, A. Christenson, et al., “Direct Electron Transfer Between Copper-Containing Proteins and Electrodes,” *Biosensors & Bioelectronics* 20 (2005): 2517–2554.

4. H. Chen, O. Simoska, K. Lim, et al., “Fundamentals, Applications, and Future Directions of Bioelectrocatalysis,” *Chemical Reviews* 120 (2020): 12903–12993.

5. I. Mateljak, E. Monza, M. F. Lucas, et al., “Increasing Redox Potential, Redox Mediator Activity, and Stability in a Fungal Laccase by Computer-Guided Mutagenesis and Directed Evolution,” *ACS Catalysis* 9 (2019): 4561–4572.

6. P. Ó Conghaile, M. Falk, D. MacAodha, et al., “Fully Enzymatic Membraneless Glucose|Oxygen Fuel Cell That Provides 0.275 mA cm^{-2} in 5 mm Glucose, Operates in Human Physiological Solutions, and Powers Transmission of Sensing Data,” *Analytical Chemistry* 88 (2016): 2156–2163.

7. S. Scheiblbrandner, E. Breslmayr, F. Csarman, et al., “Evolving Stability and PH-Dependent Activity of the High Redox Potential Botrytis Aclada Laccase for Enzymatic Fuel Cells,” *Scientific Reports* 7 (2017): 13688.

8. I. Mazurenko, T. Adachi, B. Ezraty, M. Ilbert, K. Sowa, and E. Lojou, “Electrochemistry of Copper Efflux Oxidase-Like Multicopper Oxidases Involved in Copper Homeostasis,” *Current Opinion in Electrochemistry* 32 (2022): 100919, https://doi.org/10.1016/j.coelec.2021.100919.

9. E. I. Solomon, U. M. Sundaram, and T. E. Machonkin, “Multicopper Oxidases and Oxygenases,” *Chemical Reviews* 96, no. 7 (1996): 2563–2606, https://doi.org/10.1021/cr950046o.

10. E. I. Solomon, A. J. Augustine, and J. Yoon, “O2 Reduction to H_2O by the Multicopper Oxidases,” *Dalton Transactions* 30 (2008): 3921–3932, https://doi.org/10.1039/B800799C.

11. N. Mano and A. de Poulpiquet, “O2 Reduction in Enzymatic Biofuel Cells,” *Chemical Reviews* 118 (2018): 2392–2468.

12. A. J. Augustine, M. E. Kragh, R. Sarangi, et al., “Spectroscopic Studies of Perturbed T1 Cu Sites in the Multicopper Oxidases *Saccharomyces cerevisiae* Fet3p and *Rhus vernicifera* Laccase: Allosteric Coupling Between the T1 and Trinuclear Cu Sites,” *Biochemistry* 47 (2008): 2036–2045.

13. D. W. Randall, S. D. George, B. Hedman, K. O. Hodgson, K. Fujisawa, and E. I. Solomon, “Spectroscopic and Electronic Structural Studies of Blue Copper Model Complexes. 1. Perturbation of the Thiolate–Cu Bond,” *Journal of the American Chemical Society* 122 (2000): 11620–11631.

14. D. W. Randall, S. D. George, P. L. Holland, et al., “Spectroscopic and Electronic Structural Studies of Blue Copper Model Complexes. 2. Comparison of Three- and Four-Coordinate Cu(II)–Thiolate Complexes and Fungal Laccase,” *Journal of the American Chemical Society* 122 (2000): 11632–11648.

15. S. Dong and T. G. Spiro, “Ground- and Excited-State Mapping of Plastocyanin From Resonance Raman Spectra of Isotope-Labeled Proteins,” *Journal of the American Chemical Society* 120 (1998): 10434–10440.

16. D. Qiu, S. Dong, J. Ybe, M. Hecht, and T. G. Spiro, “Variations in the Type I Copper Protein Coordination Group. Resonance Raman Spectrum of 34S-, 65Cu-, and 15N-Labeled Plastocyanin,” *Journal of the American Chemical Society* 117 (1995): 6443–6446.

17. C. R. Andrew, H. Yeom, J. S. Valentine, et al., “Raman Spectroscopy as an Indicator of Cu–S Bond Length in Type 1 and Type 2 Copper Cysteinate Proteins,” *Journal of the American Chemical Society* 116 (1994): 11489–11498.

18. B. C. Dave, J. P. Germanas, and R. S. Czernuszewicz, “The First Direct Evidence for Copper(II)-cysteine Vibrations in Blue Copper Proteins:

Resonance Raman Spectra of 34S-Cys-Labeled Azurins Reveal Correlation of Ccopper-Sulfur Stretching Frequency With Metal Site Geometry," *Journal of the American Chemical Society* 115 (1993): 12175–12176.

19. O. Siiman, N. M. Young, and P. R. Carey, "Resonance Raman Spectra of "Blue" Copper Proteins and the Nature of Their Copper Sites," *Journal of the American Chemical Society* 98 (1976): 744–748.

20. R. Cai, S. Abdellaoui, J. P. Kitt, et al., "Confocal Raman Microscopy for the Determination of Protein and Quaternary Ammonium Ion Loadings in Biocatalytic Membranes for Electrochemical Energy Conversion and Storage," *Analytical Chemistry* 89 (2017): 13290–13298.

21. S. Dong, J. A. Ybe, M. H. Hecht, and T. G. Spiro, "H-Bonding Maintains the Active Site of Type 1 Copper Proteins: Site-Directed Mutagenesis of Asn38 in Poplar Plastocyanin," *Biochemistry* 38 (1999): 3379–3385.

22. N. Kitajima, K. Fujisawa, and Y. Morooka, "Tetrahedral Copper(II) Complexes Supported by a Hindered Pyrazolylborate. Formation of the Thiolato Complex, Which Closely Mimics the Spectroscopic Characteristics of Blue Copper Proteins," *Journal of the American Chemical Society* 112 (1990): 3210–3212.

23. D. Qiu, L. Kilpatrick, N. Kitajima, and T. G. Spiro, "Modeling Blue Copper Protein Resonance Raman Spectra With Thiolate-CuII Complexes of a Sterically Hindered Tris(Pyrazolyl)borate," *Journal of the American Chemical Society* 116 (1994): 2585–2590.

24. A. Urushiyama and J. Tobari, "Resonance Raman Active Vibrations of Blue Copper Proteins. Normal Coordinate Analysis on 169-Atom Model," *Bulletin of the Chemical Society of Japan* 63 (1990): 1563–1571.

25. U. Ozuguzel, A. J. A. Aquino, R. Nieman, S. D. Minteer, and C. Korzeniewski, "Calculation of Resonance Raman Spectra and Excited State Properties for Blue Copper Protein Model Complexes," *ACS Sustainable Chemistry & Engineering* 10, no. 44 (2022): 14614–14623, https://doi.org/10.1021/acssuschemeng.2c04802.

26. C. E. Schulz, M. van Gastel, D. A. Pantazis, and F. Neese, "Converged Structural and Spectroscopic Properties for Refined QM/MM Models of Azurin," *Inorganic Chemistry* 60, no. 10 (2021): 7399–7412, https://doi.org/10.1021/acs.inorgchem.1c00640.

27. R. G. Hadt, N. Sun, N. M. Marshall, et al., "Spectroscopic and DFT Studies of Second-Sphere Variants of the Type 1 Copper Site in Azurin: Covalent and Nonlocal Electrostatic Contributions to Reduction Potentials," *Journal of the American Chemical Society* 134, no. 40 (2012): 16701–16716, https://doi.org/10.1021/ja306438n.

28. F. De Rienzo, R. R. Gabdoulline, M. C. Menziani, and R. C. Wade, "Blue Copper Proteins: A Comparative Analysis of Their Molecular Interaction Properties," *Protein Science* 9, no. 8 (2000): 1439–1454, https://doi.org/10.1110/ps.9.8.1439.

29. E. T. Adman, R. E. Stenkamp, L. C. Sieker, and L. H. Jensen, "A Crystallographic Model for Azurin at 3 Å Resolution," *Journal of Molecular Biology* 123, no. 1 (1978): 35–47, https://doi.org/10.1016/0022-2836(78)90375-3.

30. P. M. Colman, H. C. Freeman, J. M. Guss, et al., "X-Ray Crystal Structure Analysis of Plastocyanin at 2.7 Å Resolution," *Nature* 272, no. 5651 (1978): 319–324, https://doi.org/10.1038/272319a0.

31. D. F. Hansen and J. J. Led, "Determination of the Geometric Structure of the Metal Site in a Blue Copper Protein by Paramagnetic NMR," *Proceedings of the National Academy of Sciences* 103, no. 6 (2006): 1738–1743, https://doi.org/10.1073/pnas.0507179103.

32. E. N. Baker, "Structure of Azurin From *Alcaligenes denitrificans* Refinement at 1.8 Å Resolution and Comparison of the Two Crystallographically Independent Molecules," *Journal of Molecular Biology* 203, no. 4 (1988): 1071–1095, https://doi.org/10.1016/0022-2836(88)90129-5.

33. N. M. Marshall, D. K. Garner, T. D. Wilson, et al., "Rationally Tuning the Reduction Potential of a Single Cupredoxin Beyond the Natural Range," *Nature* 462, no. 7269 (2009): 113–116, https://doi.org/10.1038/nature08551.

34. E. I. Solomon, R. K. Szilagyi, S. DeBeer George, and L. Basumallick, "Electronic Structures of Metal Sites in Proteins and Models: Contributions to Function in Blue Copper Proteins," *Chemical Reviews* 104, no. 2 (2004): 419–458, https://doi.org/10.1021/cr0206317.

35. E. I. Solomon, "Spectroscopic Methods in Bioinorganic Chemistry: Blue to Green to Red Copper Sites," *Inorganic Chemistry* 45, no. 20 (2006): 8012–8025, https://doi.org/10.1021/ic060450d.

36. B. R. Crane, A. J. Di Bilio, J. R. Winkler, and H. B. Gray, "Electron Tunneling in Single Crystals of *Pseudomonas aeruginosa* Azurins," *Journal of the American Chemical Society* 123, no. 47 (2001): 11623–11631, https://doi.org/10.1021/ja0115870.

37. B. R. Crane, A. J. Di Bilio, J. R. Winkler, and H. B. Gray, *Pseudomonas aeruginosa Oxidized Azurin(Cu2+) Ru(Tpy)(Phen)(His83)* (New Brunswick, New Jersey: RCSB Protein Data Bank, 2001).

38. P. Pospíšil, J. Sýkora, K. Takematsu, M. Hof, H. B. Gray, and A. Vlček, "Light-Induced Nanosecond Relaxation Dynamics of Rhenium-Labeled *Pseudomonas aeruginosa* Azurins," *Journal of Physical Chemistry B* 124, no. 5 (2020): 788–797, https://doi.org/10.1021/acs.jpcb.9b10802.

39. J. J. Rivera, J. H. Liang, G. R. Shimamura, H. S. Shafaat, and J. E. Kim, "Raman and Quantum Yield Studies of Trp48-D5 in Azurin: Closed-Shell and Neutral Radical Species," *Journal of Physical Chemistry B* 123, no. 30 (2019): 6430–6443, https://doi.org/10.1021/acs.jpcb.9b04655.

40. N. S. Ferris, W. H. Woodruff, D. L. Tennent, and D. R. McMillin, "Native Azurin and Its Ni(II) Derivative: A Resonance Raman Study," *Biochemical and Biophysical Research Communications* 88, no. 1 (1979): 288–296, https://doi.org/10.1016/0006-291X(79)91728-5.

41. T. J. Thamann, P. Frank, L. J. Willis, and T. M. Loehr, "Normal Coordinate Analysis of the Copper Center of Azurin and the Assignment of Its Resonance Raman Spectrum," *Proceedings of the National Academy of Sciences* 79, no. 20 (1982): 6396–6400, https://doi.org/10.1073/pnas.79.20.6396.

42. S. Corni, F. De Rienzo, R. Di Felice, and E. Molinari, "Role of the Electronic Properties of Azurin Active Site in the Electron-Transfer Process," *International Journal of Quantum Chemistry* 102, no. 3 (2005): 328–342, https://doi.org/10.1002/qua.20374.

43. C. Romero-Muñiz, M. Ortega, J. G. Vilhena, et al., "Ab Initio Electronic Structure Calculations of Entire Blue Copper Azurins," *Physical Chemistry Chemical Physics* 20, no. 48 (2018): 30392–30402, https://doi.org/10.1039/C8CP06862C.

44. R. Sarangi, S. I. Gorelsky, L. Basumallick, et al., "Spectroscopic and Density Functional Theory Studies of the Blue−Copper Site in M121SeM and C112SeC Azurin: Cu−Se Versus Cu−S Bonding," *Journal of the American Chemical Society* 130, no. 12 (2008): 3866–3877, https://doi.org/10.1021/ja076495a.

45. M. A. Webb, C. N. Kiser, J. H. Richards, et al., "Resonance Raman Spectroscopy of Met121Glu Azurin," *Journal of Physical Chemistry B* 104, no. 46 (2000): 10915–10920, https://doi.org/10.1021/jp000832j.

46. Y.-S. Lin, G.-D. Li, S.-P. Mao, and J.-D. Chai, "Long-Range Corrected Hybrid Density Functionals With Improved Dispersion Corrections," *Journal of Chemical Theory and Computation* 9 (2013): 263–272.

47. F. Weigend, M. Haser, H. Patzelt, and R. Ahlrichs, "RI-MP2: Optimized Auxiliary Basis Sets and Demonstration of Efficiency," *Chemical Physics Letters* 294 (1998): 143–152.

48. C. Hattig, "Geometry Optimizations With the Coupled-Cluster Model CC2 Using the Resolution-Of-The-Identity Approximation," *Journal of Chemical Physics* 118 (2003): 7751–7761.

49. J. Tomasi, B. Mennucci, and R. Cammi, "Quantum Mechanical Continuum Solvation Models," *Chemical Reviews* 105, no. 8 (2005): 2999–3094, https://doi.org/10.1021/cr9904009.

50. F. Neese and G. Olbrich, "Efficient Use of the Resolution of the Identity Approximation in Time-Dependent Density Functional Calculations

With Hybrid Density Functionals," *Chemical Physics Letters* 362, no. 1 (2002): 170–178, https://doi.org/10.1016/S0009-2614(02)01053-9.

51. B. de Souza, F. Neese, and R. Izsák, "On the Theoretical Prediction of Fluorescence Rates From First Principles Using the Path Integral Approach," *Journal of Chemical Physics* 148, no. 3 (2018): 034104, https://doi.org/10.1063/1.5010895.

52. A. Baiardi, J. Bloino, and V. Barone, "A General Time-Dependent Route to Resonance-Raman Spectroscopy Including Franck-Condon, Herzberg-Teller and Duschinsky Effects," *Journal of Chemical Physics* 141, no. 11 (2014): 114108, https://doi.org/10.1063/1.4895534.

53. F. J. Avila Ferrer and F. Santoro, "Comparison of Vertical and Adiabatic Harmonic Approaches for the Calculation of the Vibrational Structure of Electronic Spectra," *Physical Chemistry Chemical Physics* 14, no. 39 (2012): 13549–13563, https://doi.org/10.1039/C2CP41169E.

54. P. Macak, Y. Luo, and H. Ågren, "Simulations of Vibronic Profiles in Two-Photon Absorption," *Chemical Physics Letters* 330, no. 3 (2000): 447–456, https://doi.org/10.1016/S0009-2614(00)01096-4.

55. D. C. Blazej and W. L. Peticolas, "Ultraviolet Resonance Raman Excitation Profiles of Pyrimidine Nucleotides," *Journal of Chemical Physics* 72, no. 5 (1980): 3134–3142, https://doi.org/10.1063/1.439547.

56. F. Plasser and H. Lischka, "Analysis of Excitonic and Charge Transfer Interactions From Quantum Chemical Calculations," *Journal of Chemical Theory and Computation* 8 (2012): 2777–2789.

57. F. Neese, F. Wennmohs, U. Becker, and C. Riplinger, "ORCA Quantum Chemistry Program Package," *Journal of Chemical Physics* 152 (2020): 224108.

58. F. Plasser, M. Wormit, and A. Dreuw, "New Tools for the Systematic Analysis and Visualization of Electronic Excitations. I. Formalism," *Journal of Chemical Physics* 141 (2014): 024106.

59. F. T. Plasser, "TheoDORE: A Toolbox for a Detailed and Automated Analysis of Electronic Excited State Computations," *Journal of Physical Chemistry A* 152, no. 8 (2020): 084108, https://doi.org/10.1063/1.5143076.

60. R. L. Martin, "Natural Transition Orbitals," *Journal of Chemical Physics* 118 (2003): 4775–4777.

Supporting Information

Additional supporting information can be found online in the Supporting Information section.